Commun Nonlinear Sci Numer Simulat 61 (2018) 149–159

Contents lists available at ScienceDirect

Commun Nonlinear Sci Numer Simulat

journal homepage: www.elsevier.com/locate/cnsns

Research paper

A benchmark problem for the two- and three-dimensional Cahn–Hilliard equations

Darae Jeong, Yongho Choi, Junseok Kim*

Department of Mathematics, Korea University, Seoul 02841, Republic of Korea

ARTICLE INFO

Article history:
Received 20 May 2017
Revised 21 December 2017
Accepted 6 February 2018
Available online 8 February 2018

Keywords:
Cahn–Hilliard equation
Finite difference method
Multigrid method
Benchmark problem

ABSTRACT

This paper proposes a benchmark problem for the two- and three-dimensional Cahn–Hilliard (CH) equations, which describe the process of phase separation. The CH equation is highly nonlinear and an analytical solution does not exist except trivial solutions. Therefore, we have to approximate the CH equation numerically. To test the accuracy of a numerical scheme, we have to resort to convergence tests, which consist of consecutive relative errors or a very fine solution from the numerical scheme. For a fair convergence test, we provide benchmark problems which are of the shrinking annulus and spherical shell type. We show numerical results by using the explicit Euler's scheme with a very fine time step size and also present a comparison test with Eyre's convex splitting schemes.

1. Introduction

This paper proposes a benchmark problem for the two- and three-dimensional Cahn–Hilliard (CH) equations, which were originally introduced as a mathematical model of phase separation in a binary alloy [1,2]:

$$\frac{\partial \phi(\mathbf{x},t)}{\partial t} = \Delta \mu(\phi(\mathbf{x},t)), \quad \mathbf{x} \in \Omega, \ 0 < t \le T, \tag{1}$$

$$\mu(\phi(\mathbf{x},t)) = F'(\phi(\mathbf{x},t)) - \epsilon^2 \Delta \phi(\mathbf{x},t), \tag{2}$$

where $\Omega \subset \mathbb{R}^d$ ($d = 1, 2,$ or 3) is a bounded domain, $F(\phi) = 0.25(\phi^2 - 1)^2$, and ϵ is the gradient energy coefficient. The quantity $\phi(\mathbf{x}, t)$ is defined as the difference of molar fractions of two species.

The CH equation has been applied to model many scientific processes such as phase separation and coarsening phenomena [1,3], image inpainting (the process of reconstructing lost or deteriorated parts of images) [4], image segmentation [5], multiphase fluid flows [6–9], diblock copolymer (a polymer consisting of two types of monomers) [10–12], microstructures with elastic inhomogeneity [13,14], topology optimization for optimizing material shape within a given design space and a set of loads and boundary conditions [15,16], and tumor growth simulation [17–19]. Many efficient and accurate numerical methods have been proposed to solve the CH equation. For example, the methods are meshless method [20,21], dual reciprocity method [22], Galerkin method [23–25], Fourier spectral method [26–29], unconditionally stable scheme [30–32], multigrid [16], Crank–Nicholson method [33–35], and Runge–Kutta method [36].

* Corresponding author.
E-mail address: cfdkim@korea.ac.kr (J. Kim).
URL: http://math.korea.ac.kr/~cfdkim/ (J. Kim)

https://doi.org/10.1016/j.cnsns.2018.02.006
1007-5704/

However, the CH equation is highly nonlinear due to the term $F(\phi)$ and an analytical solution does not exist except trivial constant solutions. To test the accuracy of a numerical scheme for the CH equation, we have to resort to convergence tests, which consist of consecutive relative errors or a very fine solution from the numerical scheme. The growing phase field community has developed many numerical methods; however, the lack of benchmark problems to consistently evaluate the numerical performance of the developed code [37] has been an issue. Recently, a couple of research papers have been published that are related to benchmark problems. In [38], the author has derived analytical expressions for the solution of a surface Hele–Shaw model on the sphere, to serve numerical purposes, as a benchmark for the surface CH equation. In [37], the authors presented two benchmark problems for the numerical implementation of phase field equations that model solute diffusion along with second phase growth and coarsening.

The main purpose of this paper is to present benchmark problems for testing numerical schemes for the CH equations. The two benchmark problems are of the shrinking annulus and spherical shell type. These benchmark problems will help researchers in testing the accuracy of the developed computer codes for the CH equations. We give numerical results by using the explicit Euler's scheme with a very fine time step size and we also present a comparison test with Eyre's convex splitting schemes. This paper is organized as follows. In Section 2, we describe the numerical solution algorithm. The numerical results are presented in Section 3. Some concluding remarks are presented in Section 4.

2. Numerical solution

To obtain simple benchmark solutions, we consider the CH equation in radially (2D) as well as spherically (3D) symmetric forms:

$$\phi_t(r,t) = \frac{1}{r^{d-1}}[r^{d-1}\mu_r(r,t)]_r, \quad r \in \Omega, \ t > 0, \tag{3}$$

$$\mu(r,t) = F'(\phi(r,t)) - \frac{\epsilon^2}{r^{d-1}}[r^{d-1}\phi_r(r,t)]_r, \tag{4}$$

where d is the space dimension. Here, we use the homogeneous Neumann boundary conditions for both ϕ and μ. Note that Eqs. (3) and (4) represent the radially and spherically symmetric CH equations when $d = 2$ and $d = 3$, respectively. The derivation of Eqs. (3) and (4) is described below for more detail.

- The two-dimensional Cartesian coordinate can be represented by the polar coordinate as $(x, y) = (r\cos\theta, r\sin\theta)$. In the two-dimensional polar coordinate, Eqs. (1) and (2) become

$$\frac{\partial\phi(r,\theta,t)}{\partial t} = \frac{1}{r}\frac{\partial}{\partial r}\left(r\frac{\partial\mu}{\partial r}\right) + \frac{1}{r^2}\frac{\partial^2\mu}{\partial\theta^2},$$

$$\mu(r,\theta,t) = F'(\phi) - \frac{\epsilon^2}{r}\frac{\partial}{\partial r}\left(r\frac{\partial\phi}{\partial r}\right) - \frac{\epsilon^2}{r^2}\frac{\partial^2\phi}{\partial\theta^2},$$

  where $r \geq 0, 0 \leq \theta < 2\pi$, and $0 < t \leq T$. If the solutions ϕ and μ are radially symmetric, that is, $\phi = \phi(r,t)$ and $\mu = \mu(r,t)$ are independent of θ, then $\frac{\partial^2\phi}{\partial\theta^2} = \frac{\partial^2\mu}{\partial\theta^2} = 0$. Therefore, we can obtain Eqs. (3) and (4) when $d = 2$.
- In spherical polar coordinate, $(x, y, z) = (r\sin\theta\cos\psi, r\sin\theta\sin\psi, r\cos\theta)$, Eqs. (1) and (2) become

$$\frac{\partial\phi(r,\theta,\psi,t)}{\partial t} = \frac{1}{r^2}\frac{\partial}{\partial r}\left(r^2\frac{\partial\mu}{\partial r}\right) + \frac{1}{r^2\sin^2\theta}\left[\sin\theta\frac{\partial}{\partial\theta}\left(\sin\theta\frac{\partial\mu}{\partial\theta}\right) + \frac{\partial^2\mu}{\partial\psi^2}\right],$$

$$\mu(r,\theta,\psi,t) = F'(\phi) - \frac{\epsilon^2}{r^2}\frac{\partial}{\partial r}\left(r^2\frac{\partial\phi}{\partial r}\right) - \frac{\epsilon^2}{r^2\sin^2\theta}\left[\sin\theta\frac{\partial}{\partial\theta}\left(\sin\theta\frac{\partial\phi}{\partial\theta}\right) + \frac{\partial^2\phi}{\partial\psi^2}\right],$$

  where $r \geq 0, 0 \leq \theta \leq \pi$, $0 \leq \psi < 2\pi$, and $0 < t \leq T$. Likewise, if $\phi = \phi(r,t)$ and $\mu = \mu(r,t)$ are independent of θ and ψ, that is, spherically symmetric, then we have Eqs. (3) and (4) when $d = 3$.

Now, we solve the CH Eqs. (3) and (4) in $\Omega = (0, 1)$. Let N_r be a positive integer and $h = 1/N_r$ be the uniform grid size. Let ϕ_i^n and μ_i^n be approximations of $\phi(r_i, t^n)$ and $\mu(r_i, t^n)$, respectively. Here, $r_i = (i - 0.5)h$ and $t^n = n\Delta t$. Then, we discretize Eqs. (3) and (4) in time, using the explicit Euler's method:

$$\frac{\phi_i^{n+1} - \phi_i^n}{\Delta t} = \Delta_r\mu_i^n, \ \text{for } i = 1, \ldots, N_r, \tag{5}$$

$$\mu_i^n = (\phi_i^n)^3 - \phi_i^n - \epsilon^2\Delta_r\phi_i^n. \tag{6}$$

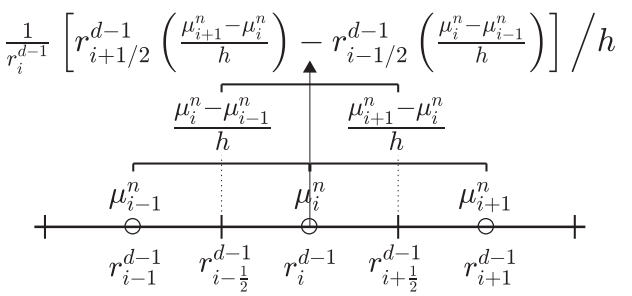

Fig. 1. Schematic illustration of discrete Laplace stencil, Eq. (7).

Here, Δ_r denotes the discrete Laplace operator in radially and spherically symmetric coordinates. In this study, we use the following standard discrete Laplace stencil [39]:

$$\Delta_r \mu_i^n = \frac{1}{r_i^{d-1}}\left[r_{i+1/2}^{d-1}\left(\frac{\mu_{i+1}^n-\mu_i^n}{h}\right)-r_{i-1/2}^{d-1}\left(\frac{\mu_i^n-\mu_{i-1}^n}{h}\right)\right]\Big/h, \tag{7}$$

where $r_{i+1/2}^{d-1}=(r_i^{d-1}+r_{i+1}^{d-1})/2$. See Fig. 1 for a schematic illustration.

Also, the boundary condition is defined as $\phi_0^n=\phi_1^n$, $\phi_{N_r+1}^n=\phi_{N_r}^n$, $\mu_0^n=\mu_1^n$, and $\mu_{N_r+1}^n=\mu_{N_r}^n$ for all n. Note that the numerical solution from Eqs. (5) to (6) satisfy total mass conservation, that is, $\sum_{i=1}^{N_r}2(d-1)\pi(r_ih)^{d-1}\phi_i^{n+1}=\sum_{i=1}^{N_r}2(d-1)\pi(r_ih)^{d-1}\phi_i^n$ for all n. We can show this property as follows: By multiplying both sides in Eq. (5) with $2(d-1)\pi(r_ih)^{d-1}$ and summing this with respect to i, we obtain

$$\begin{aligned}\sum_{i=1}^{N_r}\frac{\phi_i^{n+1}-\phi_i^n}{\Delta t}(r_ih)^{d-1} &= \sum_{i=1}^{N_r}h^{d-3}\left[r_{i+1/2}^{d-1}(\mu_{i+1}^{n+1}-\mu_i^{n+1})-r_{i-1/2}^{d-1}(\mu_i^{n+1}-\mu_{i-1}^{n+1})\right]\\ &= h^{d-3}\left[r_{N_r+1/2}^{d-1}(\mu_{N_r+1}^{n+1}-\mu_{N_r}^{n+1})-r_{1/2}^{d-1}(\mu_1^{n+1}-\mu_0^{n+1})\right]=0,\end{aligned}$$

where the homogeneous Neumann boundary condition is used. Therefore, we can see the total mass conservation property of the numerical solution.

3. Numerical results

3.1. Benchmark problems

In this section, we provide the benchmark problems for the CH equations. We use the following simulation parameters, $N_r=64$, $h=1/N_r$, and $\Delta t=10h^4$. In this study, we consider the fourth order nonlinear CH equation with the explicit Euler's method, which is conditionally stable [40]. With the following parameters ϵ_8 and $h=1/64$ on $\Omega=(0,1)$, we found that the stable time steps are restricted by $\Delta t\le 120h^4$. Therefore, for the accuracy reason, we use a small enough time step size, $\Delta t=10h^4$, for the stable benchmark solution.

The initial state is assumed to be

$$\phi(r,0)=\tanh\left(\frac{0.1-|r-0.75|}{\sqrt{2}\epsilon}\right), \tag{8}$$

where $\epsilon=8h/[2\sqrt{2}\tanh^{-1}(0.9)]\approx 0.030019$ is assumed and its value implies that we have approximately 8 grid spacing across interfacial transition layer [41]. Unless otherwise specified, we will use this value throughout this paper.

3.1.1. Radially symmetric CH equation

First, we consider Eqs. (5) and (6) with an initial annulus shape in the two-dimensional space, i.e., $d=2$.

Fig. 2(a) shows the temporal evolution of the phase-field $\phi(r,t)$ up to $T=4{,}000{,}000\Delta t$. As time goes by, we can observe that phase moves radially inward.

Here, we define the two positions, R_1 and R_2 ($R_1>R_2$), which satisfy $\phi(R_1,t)=\phi(R_2,t)=0$ as shown in Fig. 3. Then, we call R_1 and R_2 the outer and inner radii, respectively.

To find R_1 and R_2 values, we first find two indices m_1 and m_2 ($m_1>m_2$) which satisfy $\phi_{m_1}^n\phi_{m_1+1}^n\le 0$ and $\phi_{m_2}^n\phi_{m_2+1}^n\le 0$. And then define outer and inner radii $R_1=r_{m_1}-h\phi_{m_1}/(\phi_{m_1+1}-\phi_{m_1})$ and $R_2=r_{m_2}-h\phi_{m_2}/(\phi_{m_2+1}-\phi_{m_2})$ using the linear interpolation (see Fig. 3).

In Fig. 2(b), we can observe the temporal evolution of the radii of an annulus shape up to time T. As annulus shrinks, its corresponding radii decrease.

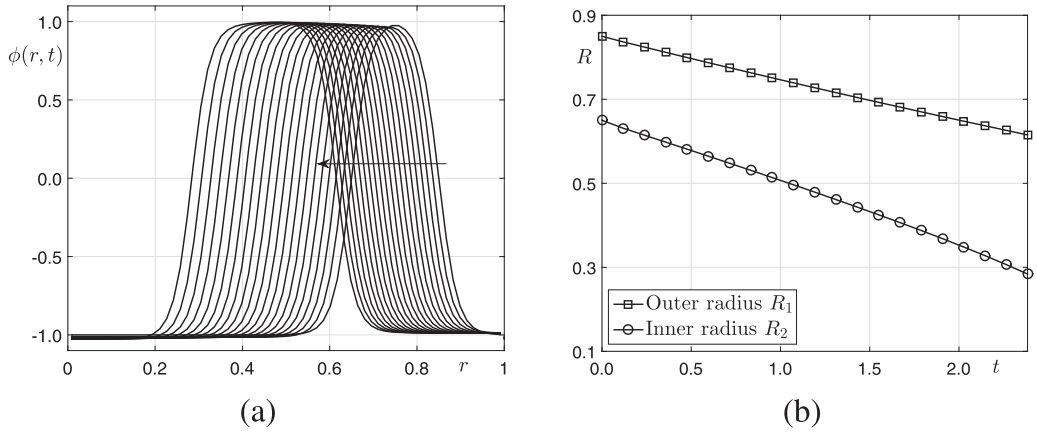

Fig. 2. Temporal evolution of (a) the phase-field ϕ and (b) the radii, R_1 and R_2, of an annulus shape.

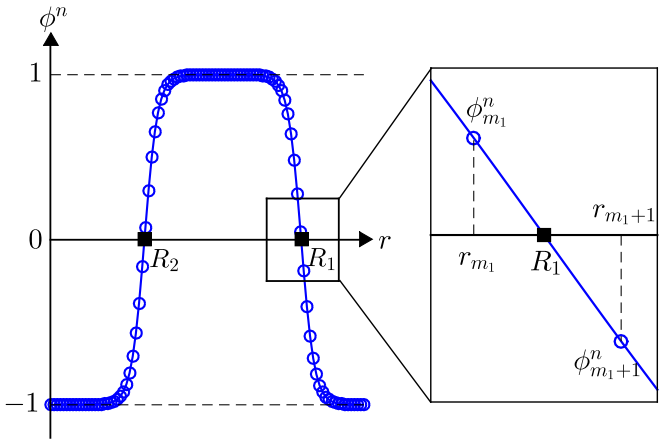

Fig. 3. Schematic illustration of the outer and inner radii R_1 and R_2 such that $\phi(R_1) = \phi(R_2) \approx 0$.

Table 1
Numerical solution ϕ at $T = 4,000,000\Delta t \approx 2.384185791015625$.

$\phi_1 = -1.027504511776$	$\phi_{17} = -0.564487217154$	$\phi_{33} = 0.988605076047$	$\phi_{49} = -0.983853795737$
$\phi_2 = -1.027498725129$	$\phi_{18} = -0.250859935848$	$\phi_{34} = 0.976057569899$	$\phi_{50} = -0.985170594999$
$\phi_3 = -1.027484177921$	$\phi_{19} = 0.121508898697$	$\phi_{35} = 0.949235589084$	$\phi_{51} = -0.985815573656$
$\phi_4 = -1.027453469700$	$\phi_{20} = 0.456286812712$	$\phi_{36} = 0.894926141320$	$\phi_{52} = -0.986132065568$
$\phi_5 = -1.027391123778$	$\phi_{21} = 0.691564085583$	$\phi_{37} = 0.790535176743$	$\phi_{53} = -0.986287947498$
$\phi_6 = -1.027265860219$	$\phi_{22} = 0.831789202458$	$\phi_{38} = 0.604972051322$	$\phi_{54} = -0.986365246130$
$\phi_7 = -1.027014786075$	$\phi_{23} = 0.908171459654$	$\phi_{39} = 0.316298793368$	$\phi_{55} = -0.986404031941$
$\phi_8 = -1.026511266173$	$\phi_{24} = 0.948229985036$	$\phi_{40} = -0.047136487092$	$\phi_{56} = -0.986423880370$
$\phi_9 = -1.025499705042$	$\phi_{25} = 0.969213404538$	$\phi_{41} = -0.395381379124$	$\phi_{57} = -0.986434356499$
$\phi_{10} = -1.023463352746$	$\phi_{26} = 0.980539743388$	$\phi_{42} = -0.652635247975$	$\phi_{58} = -0.986440135808$
$\phi_{11} = -1.019357592452$	$\phi_{27} = 0.987023989568$	$\phi_{43} = -0.810416052062$	$\phi_{59} = -0.986443505066$
$\phi_{12} = -1.011078093531$	$\phi_{28} = 0.991025054790$	$\phi_{44} = -0.897085623619$	$\phi_{60} = -0.986445583798$
$\phi_{13} = -0.994428189172$	$\phi_{29} = 0.993620193637$	$\phi_{45} = -0.941962689380$	$\phi_{61} = -0.986446920884$
$\phi_{14} = -0.961230919942$	$\phi_{30} = 0.995170132055$	$\phi_{46} = -0.964512120376$	$\phi_{62} = -0.986447785876$
$\phi_{15} = -0.896344006399$	$\phi_{31} = 0.995516163527$	$\phi_{47} = -0.975676021778$	$\phi_{63} = -0.986448311013$
$\phi_{16} = -0.774692830013$	$\phi_{32} = 0.993904512330$	$\phi_{48} = -0.981164203364$	$\phi_{64} = -0.986448559944$

As a reference, we present the numerical solution at $T = 4{,}000{,}000\Delta t \approx 2.384185791015625$ in Table 1. Here, we list the numerical solution ϕ_i at each grid point r_i. In addition, Table 2 shows the outer radius R_1 and the inner radius R_2 of the annulus shape at $T = t^n = n\Delta t$.

3.1.2. Spherically symmetric CH equation

Next, we consider Eqs. (5) and (6) with a initial spherical shell in the three-dimensional space, i.e., $d = 3$.

Table 2
Outer radius R_1 and inner radius R_2 of the annulus shape at time t^n.

n	R_1	R_2	n	R_1	R_2
0	0.849949775928	0.650050224072	2, 200, 000	0.715853459661	0.461200493142
200, 000	0.836608652655	0.631005604629	2, 400, 000	0.704210066169	0.443212910139
400, 000	0.824165646808	0.614467922799	2, 600, 000	0.692702600176	0.425020719886
600, 000	0.811713839369	0.597901409161	2, 800, 000	0.681469817957	0.406556929895
800, 000	0.799325779107	0.581260935303	3, 000, 000	0.670197339726	0.387714827449
1, 000, 000	0.787091221175	0.564534192377	3, 200, 000	0.658933164532	0.368317756760
1, 200, 000	0.775077346084	0.547706818509	3, 400, 000	0.647888500199	0.348304709234
1, 400, 000	0.763046909712	0.530760837096	3, 600, 000	0.637011986155	0.327830429530
1, 600, 000	0.751022358818	0.513673213674	3, 800, 000	0.626025964192	0.306482326034
1, 800, 000	0.739121856219	0.496413671465	4, 000, 000	0.615160983450	0.283963854877
2, 000, 000	0.727474182030	0.478941455356			

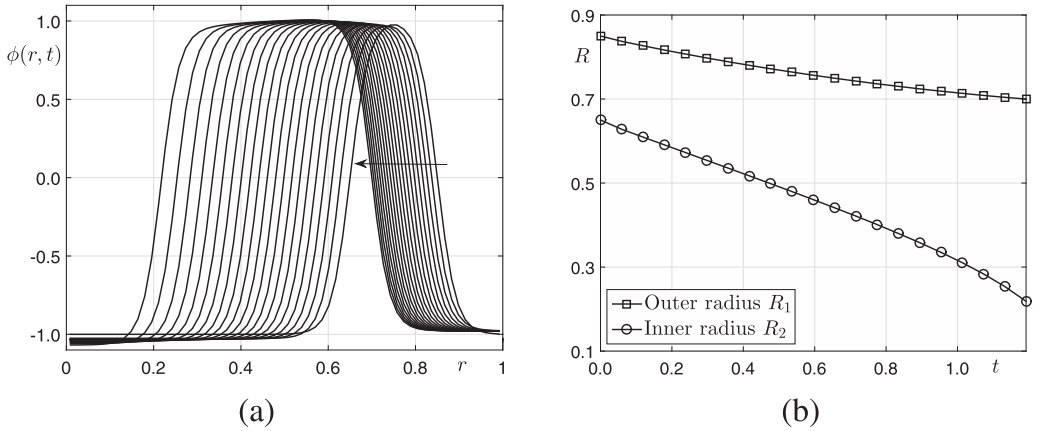

Fig. 4. Temporal evolution of (a) the phase-field ϕ and (b) the radii, R_1 and R_2, of a spherical shell shape.

Table 3
Numerical solution ϕ at $T = 2{,}000{,}000\Delta t \approx 1.192092895507813$.

$\phi_1 = -1.068084980096$	$\phi_{17} = 0.705776144838$	$\phi_{33} = 1.003261060134$	$\phi_{49} = -0.860686319005$
$\phi_2 = -1.067949971042$	$\phi_{18} = 0.827339820108$	$\phi_{34} = 1.004833794802$	$\phi_{50} = -0.919120188681$
$\phi_3 = -1.067561020556$	$\phi_{19} = 0.894195937011$	$\phi_{35} = 1.005960524410$	$\phi_{51} = -0.948760758857$
$\phi_4 = -1.066767700322$	$\phi_{20} = 0.930573780490$	$\phi_{36} = 1.006316793214$	$\phi_{52} = -0.963504268526$
$\phi_5 = -1.065231898221$	$\phi_{21} = 0.950985761219$	$\phi_{37} = 1.005234082599$	$\phi_{53} = -0.970768441032$
$\phi_6 = -1.062274217729$	$\phi_{22} = 0.963216657115$	$\phi_{38} = 1.001352427409$	$\phi_{54} = -0.974331498760$
$\phi_7 = -1.056548591713$	$\phi_{23} = 0.971239357857$	$\phi_{39} = 0.991934425656$	$\phi_{55} = -0.976075644968$
$\phi_8 = -1.045400651766$	$\phi_{24} = 0.977039639032$	$\phi_{40} = 0.971559832319$	$\phi_{56} = -0.976928721304$
$\phi_9 = -1.023650913731$	$\phi_{25} = 0.981606057073$	$\phi_{41} = 0.929841374677$	$\phi_{57} = -0.977345866119$
$\phi_{10} = -0.981462092797$	$\phi_{26} = 0.985435130155$	$\phi_{42} = 0.848204966486$	$\phi_{58} = -0.977549846106$
$\phi_{11} = -0.901277666631$	$\phi_{27} = 0.988781795973$	$\phi_{43} = 0.698177190801$	$\phi_{59} = -0.977649593104$
$\phi_{12} = -0.755888296946$	$\phi_{28} = 0.991781721504$	$\phi_{44} = 0.450466519889$	$\phi_{60} = -0.977698353914$
$\phi_{13} = -0.515852508923$	$\phi_{29} = 0.994510335027$	$\phi_{45} = 0.108434401114$	$\phi_{61} = -0.977722144585$
$\phi_{14} = -0.179783101083$	$\phi_{30} = 0.997010586595$	$\phi_{46} = -0.257726814048$	$\phi_{62} = -0.977733654081$
$\phi_{15} = 0.189363768348$	$\phi_{31} = 0.999304601478$	$\phi_{47} = -0.555412819598$	$\phi_{63} = -0.977739024097$
$\phi_{16} = 0.498347347266$	$\phi_{32} = 1.001395588233$	$\phi_{48} = -0.749933578888$	$\phi_{64} = -0.977741131595$

Fig. 4(a) represents the temporal evolution of the phase-field $\phi(r, t)$ up to $T = 2{,}000{,}000\Delta t$. Also, we observe the temporal evolutions of the radii R_1 and R_2 of the initial spherical shell up to time T in Fig. 4(b).

For reference, Table 3 shows the numerical solution ϕ_i $(i = 1, \cdots, 64)$ at $T = 2,000,000\Delta t \approx 1.192092895507813$.

Table 4 also shows the outer radius R_1 and the inner radius R_2 of the spherical shell shape at time $T = t^n = n\Delta t$.

3.2. Convergence test on two-dimensional space

Now, we implement the convergence test on two-dimensional space with the benchmark solution. For the numerical test, we use the following parameters, $h = 1/64$ and $\Delta t = 100{,}000h^4 \times 2^{-m}$ for $m = 0, 1, \ldots, 5$. In the computational domain $\Omega = (-1,\ 1) \times (-1,\ 1)$, we define the following cell-centered point (x_i, y_j), where $x_i = -1 + (i - 0.5)h$ and $y_j = -1 + (j - 0.5)h$ for $i, j = 1, 2, \ldots, 128$.

Table 4
Outer radius R_1 and inner radius R_2 of the spherical shell at time t^n.

n	R_1	R_2	n	R_1	R_2
0	0.849949775928	0.650050224072	1, 100, 000	0.749566160297	0.441094263588
100, 000	0.837323694919	0.627926360803	1, 200, 000	0.742740402958	0.421394162858
200, 000	0.826811289499	0.609358492100	1, 300, 000	0.736207511480	0.401106829486
300, 000	0.816609600079	0.590927146279	1, 400, 000	0.730154296251	0.379954281355
400, 000	0.807052995185	0.572483321272	1, 500, 000	0.724167270531	0.358182397141
500, 000	0.797674944445	0.553956623078	1, 600, 000	0.718728204566	0.335027456803
600, 000	0.788737081934	0.535482884493	1, 700, 000	0.713584293866	0.310549325671
700, 000	0.780245116282	0.517016467259	1, 800, 000	0.708565628611	0.283686304333
800, 000	0.771963227501	0.498452156823	1, 900, 000	0.704071353188	0.253694261720
900, 000	0.764227811704	0.479663429112	2, 000, 000	0.699939662701	0.218547237985
1, 000, 000	0.756643381504	0.460495290928			

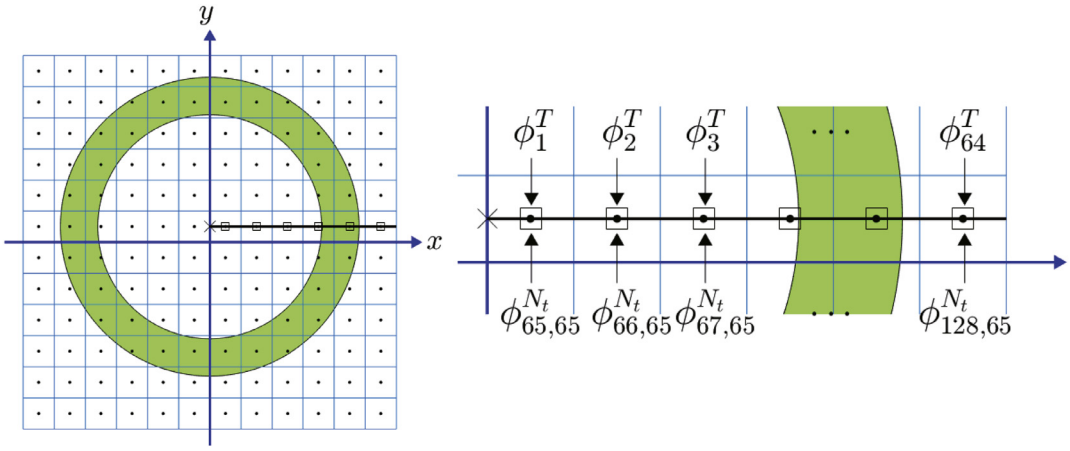

Fig. 5. Schematic illustration of the two-dimensional Cartesian coordinate. Here, square ('□') and dot ('·') symbols denote benchmark solution (ϕ_i^T) and numerical solution ($\phi_{ij}^{N_t}$), respectively.

Let ϕ_{ij}^n be approximations of $\phi(x_i, y_j, n\Delta t)$, where $\Delta t = T/N_t$ is the time step, T is the final time, and N_t is the total number of time steps.

We take the following two schemes by Eyre [40,42] as test problems. One is a nonlinearly stabilized splitting scheme:

$$\frac{\phi_{ij}^{n+1} - \phi_{ij}^n}{\Delta t} = \Delta_h \mu_{ij}^{n+1}, \tag{9}$$

$$\mu_{ij}^{n+1} = F'(\phi_{ij}^{n+1}) + \phi_{ij}^{n+1} - \phi_{ij}^n - \epsilon^2 \Delta_h \phi_{ij}^{n+1} \tag{10}$$

and the other is a linearly stabilized splitting scheme:

$$\frac{\phi_{ij}^{n+1} - \phi_{ij}^n}{\Delta t} = \Delta_h \mu_{ij}^{n+1}, \tag{11}$$

$$\mu_{ij}^{n+1} = F'(\phi_{ij}^n) - 2\phi_{ij}^n + 2\phi_{ij}^{n+1} - \epsilon^2 \Delta_h \phi_{ij}^{n+1}. \tag{12}$$

Here, $\Delta_h \psi_{ij} = (\psi_{i-1,j} + \psi_{i+1,j} + \psi_{i,j-1} + \psi_{i,j+1} - 4\psi_{ij})/h^2$. We solve these discrete equations by using a full approximation storage (FAS) multigrid method with a Gauss–Seidel relaxation [9,43,44]. The initial condition is set to be

$$\phi(x_i, y_j, 0) = \tanh \frac{0.1 - |\sqrt{x_i^2 + (y_j - 0.5h)^2} - 0.75|}{\sqrt{2}\epsilon}. \tag{13}$$

Note that we define the initial condition as the circle with the center $(0, 0.5h)$ for comparison with the benchmark solution and the test numerical solution. See Fig. 5.

To investigate the quantitative convergence, let us define the error of the numerical solution as $\mathbf{e}^T = (e_1^T, e_2^T, \cdots, e_{64}^T)$, where $e_i^T = \phi_{64+i,65}^{N_t} - \phi_i^T$ for $i = 1, 2, \cdots, 64$. Here, $\phi_{64+i,65}^{N_t}$ and ϕ_i^T denote the numerical and benchmark solutions at $T = N_t \Delta t$, respectively. For a better understanding, we present the schematic illustration in Fig. 5.

Here, we consider the following discrete norm of error as

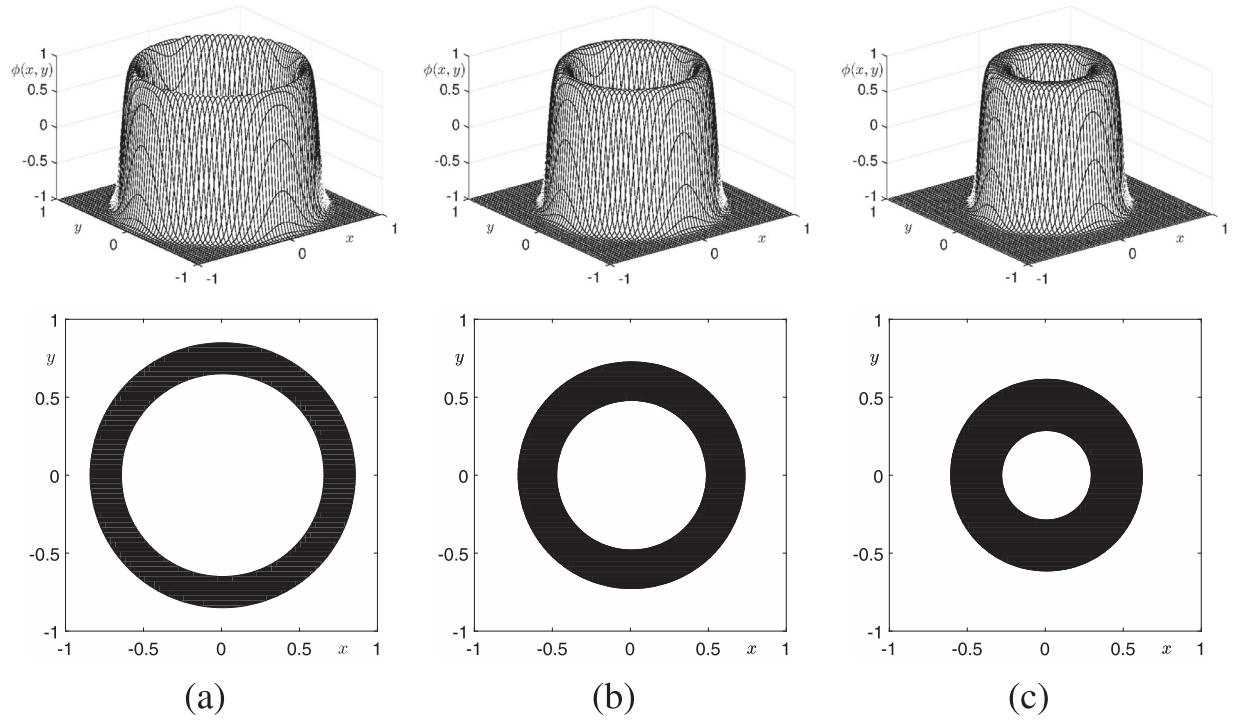

Fig. 6. Columns (a)–(c) are snapshots of the numerical solutions at $t = 0,\ 1.311$, and 2.38, respectively. The top row is a mesh view whereas the bottom row is a filled contour at level zero.

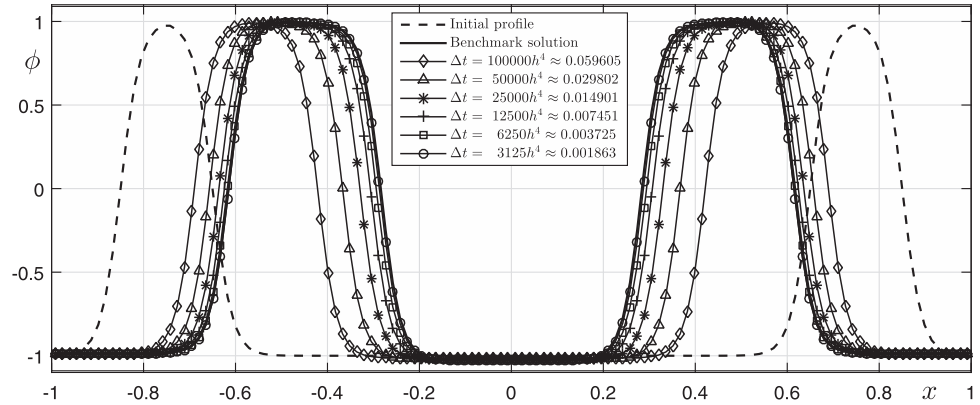

Fig. 7. Numerical solutions using the nonlinear splitting scheme with six different time steps at $T = 40{,}000{,}000h^4 \approx 2.3842$.

- the discrete l_2-norm:

$$\| \mathbf{e}^T \|_2 = \sqrt{2(d-1)\pi \sum_{i=1}^{64} \left(e_i^T\right)^2 (r_i)^{d-1} h}, \tag{14}$$

- the discrete maximum norm:

$$\|\mathbf{e}^T\|_\infty = \max_{1 \le i \le 64} |e_i^T|, \tag{15}$$

where d is the dimension of the Cartesian domain.

Fig. 6(a)–(c) are snapshots of the numerical solutions of Eqs. (9) and (10) with $\Delta t = 3125h^4$ at $t = 0,\ 1.311$, and 2.38, respectively. Top row is a mesh view and bottom row is a filled contour at level zero.

Fig. 7 shows the numerical solutions using the nonlinear splitting scheme with six different time steps. We can observe the convergence of the solutions to the benchmark solution as we refine the time step.

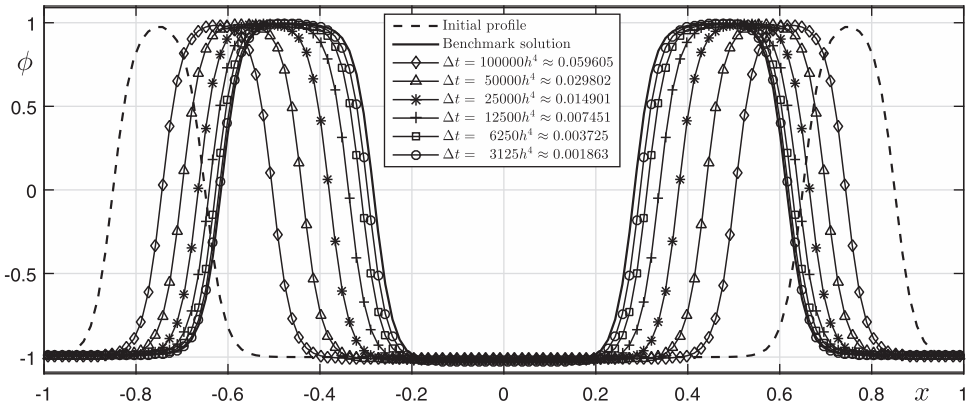

Fig. 8. Numerical solutions using the linear splitting scheme with six different time steps at $T = 40{,}000{,}000h^4 \approx 2.3842$.

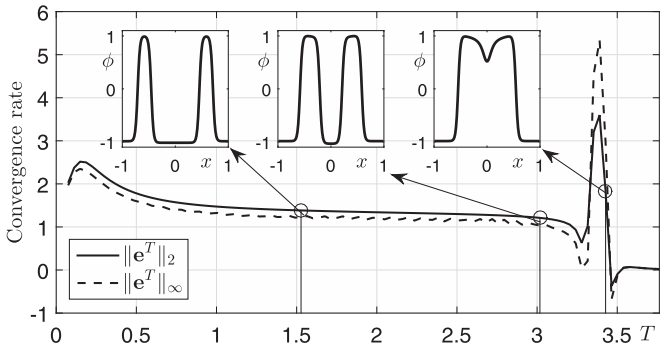

Fig. 9. Temporal change of convergence rates (fifth column in Table 5) for numerical solution by the nonlinear scheme.

Table 5
Convergence of numerical results by the nonlinear splitting scheme with respect to time step size Δt at $T = 100{,}000h^4$.

Case(Δt)	$25{,}000h^4$	Rate	$12{,}500h^4$	Rate	$6250h^4$	Rate	$3125h^4$
$\|\mathbf{e}^T\|_2$	0.006187	0.936	0.003233	1.162	0.001445	1.470	0.000521
$\|\mathbf{e}^T\|_\infty$	0.009921	1.034	0.004844	1.368	0.001877	1.692	0.000581

Table 6
Convergence of numerical results by the linear splitting scheme with respect to time step size Δt at $T = 100{,}000h^4$.

Case(Δt)	$25{,}000h^4$	Rate	$12{,}500h^4$	Rate	$6250h^4$	Rate	$3125h^4$
$\|\mathbf{e}^T\|_2$	0.010947	0.705	0.006717	0.907	0.003582	1.138	0.001628
$\|\mathbf{e}^T\|_\infty$	0.019238	0.748	0.011455	0.958	0.005898	1.239	0.002499

Table 5 shows the discrete l_2 norm $\|\mathbf{e}^T\|_2$ and maximum norm $\|\mathbf{e}^T\|_\infty$ of the errors and rates of convergence for the results with $m = 2, 3, 4, 5$. This result suggests that the scheme is approximately first-order accurate in time.

Fig. 8 and Table 6 show the results using the linearly stabilized splitting scheme. The scheme also converges with approximately first-order accuracy, with though the accurate less than that of the nonlinearly stabilized splitting scheme.

If we calculate the convergence rates (the fifth column in Table 5) of the numerical solutions by the nonlinear scheme for a long time, then we obtain the following results as shown in Fig. 9. Therefore, the maximum value for the stable results is approximately up to $T = 3$.

3.3. Convergence test on three-dimensional space

As the final test, we implement a convergence test on three-dimensional space $\Omega = (-1, 1)^3$. As in the previous section, we define the cell-centered points (x_i, y_j, z_k), where $x_i = -1 + (i - 0.5)h$, $y_j = -1 + (j - 0.5)h$, and $z_k = -1 + (k - 0.5)h$ for $i, j, k = 1, 2, \cdots, N_x$. The other numerical parameters are given as $N_x = 64$, $h = 1/N_x$, $T = 20{,}000{,}000h^4$, and $\Delta t =$

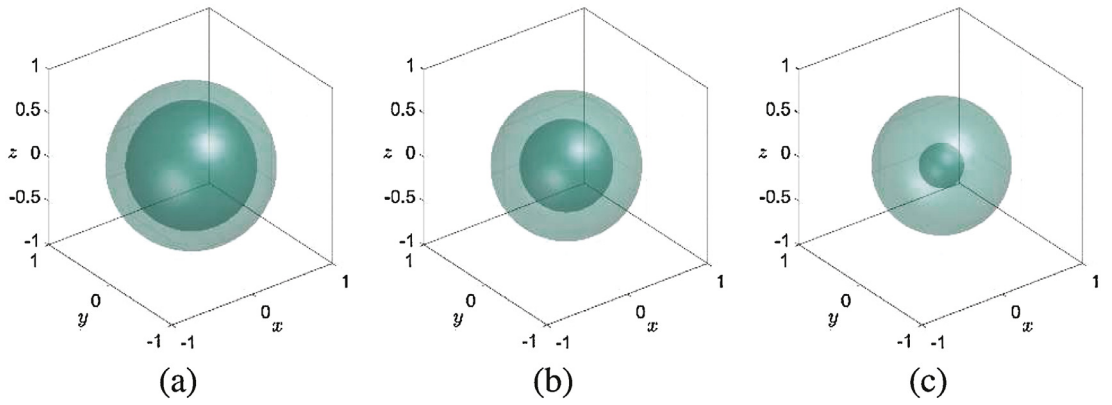

Fig. 10. Numerical solutions by the nonlinear splitting method at (a) $t = 0$, (b) $t = 0.596$, and (c) $t = 1.192$, respectively.

Table 7
Convergence of numerical results by the nonlinear splitting scheme with respect to time step size Δt at $T = 100{,}000h^4$.

Case(Δt)	$25{,}000h^4$	Rate	$125{,}000h^4$	Rate	$6250h^4$	Rate	$3125h^4$
$\|\mathbf{e}^T\|_2$	0.014882	0.931	0.007804	1.121	0.003587	1.118	0.001653
$\|\mathbf{e}^T\|_\infty$	0.019943	1.014	0.009873	1.352	0.003867	1.233	0.001646

$100{,}000h^4 \times 2^{-m}$ for $m = 1, 2, 3, 4$. The initial condition is given by

$$\phi(x, y, z, 0) = \tanh \frac{0.1 - |\sqrt{x^2 + (y - 0.5h)^2 + (z - 0.5h)^2} - 0.75|}{\sqrt{2}\epsilon}. \tag{16}$$

Let ϕ_{ijk}^n be approximations of $\phi(x_i, y_j, z_k, n\Delta t)$, where $\Delta t = T/N_t$ is the time step, T is the final time, and N_t is the total number of time steps.

We consider the discrete fully three-dimensional CH equation with nonlinearly and linearly stabilized splitting schemes [40,42] as follows.

• Nonlinearly stabilized splitting scheme:

$$\frac{\phi_{ijk}^{n+1} - \phi_{ijk}^n}{\Delta t} = \Delta_h \mu_{ijk}^{n+1}, \tag{17}$$

$$\mu_{ijk}^{n+1} = F'(\phi_{ijk}^{n+1}) + \phi_{ijk}^{n+1} - \phi_{ijk}^n - \epsilon^2 \Delta_h \phi_{ijk}^{n+1}, \tag{18}$$

• Linearly stabilized splitting scheme:

$$\frac{\phi_{ijk}^{n+1} - \phi_{ijk}^n}{\Delta t} = \Delta_h \mu_{ijk}^{n+1}, \tag{19}$$

$$\mu_{ijk}^{n+1} = F'(\phi_{ijk}^n) - 2\phi_{ijk}^n + 2\phi_{ijk}^{n+1} - \epsilon^2 \Delta_h \phi_{ijk}^{n+1}. \tag{20}$$

Here, $\Delta_h \psi_{ijk} = (\psi_{i-1,jk} + \psi_{i+1,jk} + \psi_{i,j-1,k} + \psi_{i,j+1,k} + \psi_{ij,k-1} + \psi_{ij,k+1} - 6\psi_{ijk})/h^2$. Also, we solve these equations with the multigrid method.

Fig. 10(a)–(c) show the numerical solutions by nonlinear splitting method at $t = 0$, $t = 0.596$, and $t = 1.192$, respectively.

Fig. 11 shows the numerical solutions by the nonlinear splitting scheme with four different time steps at $T = 20{,}000{,}000h^4$. We can observe the convergence of the solutions to the benchmark solution as we refine the time step. Next, for the quantitative convergence, we define the error of the numerical solution as $\mathbf{e}^T = (e_1^T, e_2^T, \cdots, e_{64}^T)$, where $e_i^T = \phi_{64+i,65,65}^{N_t} - \phi_i^T$ for $i = 1, 2, \cdots, 64$. Here, $\phi_{64+i,65,65}^{N_t}$ and ϕ_i^T denote the numerical and benchmark solutions at $T = N_t \Delta t$, respectively. Table 7 shows the discrete l_2 norm $\|\mathbf{e}^T\|_2$ and maximum norm $\|\mathbf{e}^T\|_\infty$ of the errors and rates of convergence for the results at $T = 100,000h^4$ with respect to time step size. This result suggests that the scheme is approximately first-order accurate in time.

Fig. 12 and Table 8 show the results using the linearly stabilized splitting scheme. The scheme also converges approximately with first-order accuracy, though the accuracy is less than that of the nonlinearly stabilized splitting scheme.

If we use a relatively large time step, then from these results we can observe the huge deviations of the tested CH implementations among each others and from the benchmark problem. This shows that many numerical implementations

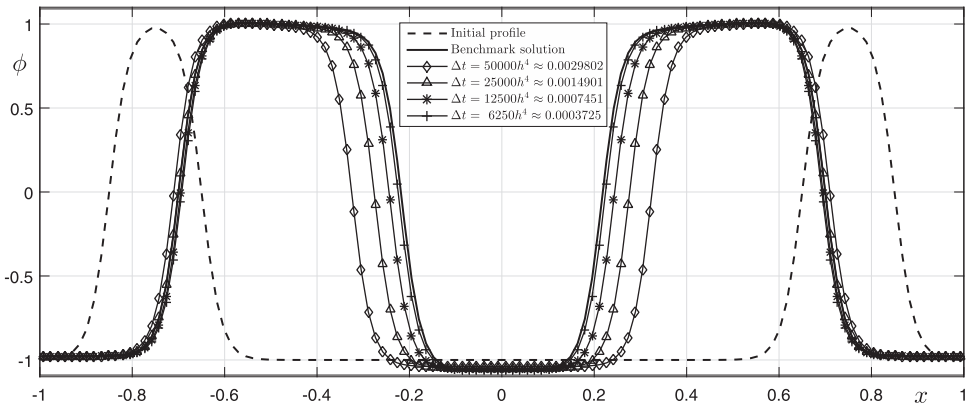

Fig. 11. Numerical solutions using the nonlinear splitting scheme with four different time steps at $T = 20{,}000{,}000h^4 \approx 1.1921$.

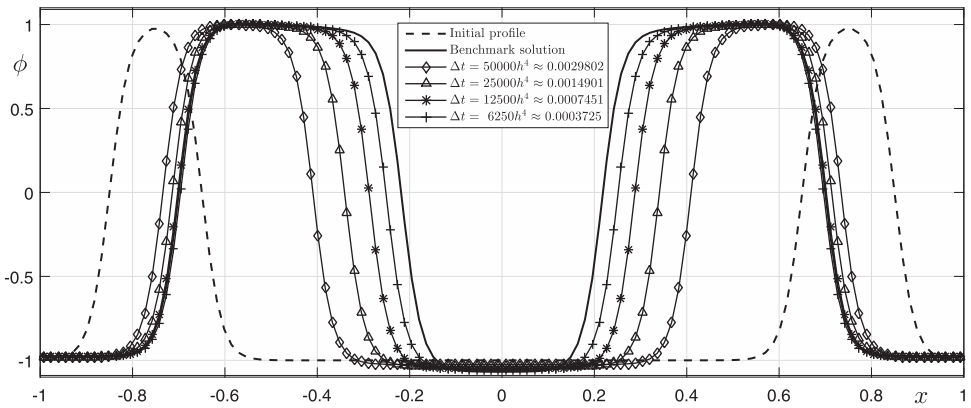

Fig. 12. Numerical solutions using the linear splitting scheme with four different time steps at $T = 20{,}000{,}000h^4 \approx 1.1921$.

Table 8
Convergence of numerical results by the linear splitting scheme with respect to time step size Δt at $T = 100{,}000h^4$.

Case(Δt)	$25{,}000h^4$	Rate	$12{,}500h^4$	Rate	$6250h^4$	Rate	$3125h^4$
$\|\mathbf{e}^T\|_2$	0.026396	0.704	0.016199	0.907	0.008638	1.114	0.003990
$\|\mathbf{e}^T\|_\infty$	0.038912	0.729	0.023469	0.943	0.012205	1.226	0.005217

can reflect the CH equation qualitatively but not quantitatively. It also shows how important the development of benchmark problems for the CH equation is, taking into account the large field of applications where this equation is included.

Note that we can generate other benchmark solutions with different grid sizes, initial conditions, and final times for a benchmark problem because Eq. (6) is explicit and simple. Also note that typically, the convergence tests were performed with a short final time.

4. Concluding remarks

In this work, we presented a benchmark problem for the two- and three-dimensional CH equations. The benchmark problems are shrinking annulus and spherical shell domains and we obtain numerical results for the CH equation by using the explicit Euler's scheme with a very fine time step size. With this numerical solution we can test a temporal discretization of the numerical scheme. As a test problem, we performed a comparison study with Eyre's nonlinear and linear convex splitting schemes. The computational results showed that the nonlinear convex splitting scheme is much better than the linear one in terms of accuracy, when the time step is the same. The proposed method is general, and therefore can be applied to other numerical schemes such as the Fourier spectral method, finite volume, and finite element method. The proposed future work is to design a benchmark problem for a two-phase fluid flow model which consists of the Cahn–Hilliard equation and the Navier–Stokes equation. For example, diffuse interface models for incompressible two-phase flow with large density ratios were tested on benchmark configurations for a two-dimensional bubble rising in liquid columns [45].

Acknowledgments

The authors thank the reviewers for the constructive and helpful comments on the revision of this article. The first author (D. Jeong) was supported by the National Research Foundation of Korea (NRF) grant funded by the Korea government (MSIP) (NRF-2017R1E1A1A03070953). The corresponding author (J.S. Kim) was supported by Basic Science Research Program through the National Research Foundation of Korea(NRF) funded by the Ministry of Education (NRF-2016R1D1A1B03933243).

References

[1] Cahn JW. On spinodal decomposition. Acta Metall 1961;9:795–801.
[2] Cahn JW, Hilliard JE. Free energy of a non-uniform system. I. Interfacial free energy. J Chem Phys 1958;28:258–67.
[3] Maraldi M, Molari L, Grandi L. A unified thermodynamic framework for the modelling of diffusive and displacive phase transitions. Int J Eng Sci 2012;50:31–45.
[4] Bertozzi AL, Esedoglu S, Gillette A. Inpainting of binary images using the Cahn–Hilliard equation. IEEE T Image Process 2007;16:285–91.
[5] Zanetti M, Ruggiero V, Miranda M Jr. Numerical minimization of a second-order functional for image segmentation. Commun Nonlinear Sci Numer Simul 2016;36:528–48.
[6] Badalassi VE, Ceniceros HD, Banerjee S. Computation of multiphase systems with phase field models. J Comput Phys 2003;190:371–97.
[7] Heida M. On the derivation of thermodynamically consistent boundary conditions for the Cahn–Hilliard–Navier–Stokes system. Int J Eng Sci 2013;62:126–56.
[8] Kotschote M, Zacher R. Strong solutions in the dynamical theory of compressible fluid mixtures. Math Mod Meth Appl S 2015;25:1217–56.
[9] Li Y, Choi JI, Kim J. A phase-field fluid modeling and computation with interfacial profile correction term. Commun Nonlinear Sci Numer Simul 2016;30:84–100.
[10] Choksi R, Peletier MA, Williams JF. On the phase diagram for microphase separation of diblock copolymers: an approach via a nonlocal Cahn–Hilliard functional. SIAM J Appl Math 2009;69:1712–38.
[11] Jeong D, Lee S, Choi Y, Kim JS. Energy-minimizing wavelengths of equilibrium states for diblock copolymers in the hex-cylinder phase. Curr Appl Phys 2015;15:799–804.
[12] Jeong D, Shin J, Li Y, Choi Y, Jung J, Lee S, Kim JS. Numerical analysis of energy-minimizing wavelenghts of equilibrium states for diblock copolymers. Curr Appl Phys 2014;14:1263–72.
[13] Zaeem MA, Kadiri HE, Horstemeyer MF, Khafizov M, Utegulov Z. Effects of internal stresses and intermediate phases on the coarsening of coherent precipitates: a phase-field study. Curr Appl Phys 2012;12:570–80.
[14] Zhu J, Chen LQ, Shen J. Morphological evolution during phase separation and coarsening with strong inhomogeneous elasticity. Model Simul Mater Sci Eng 2001;9:499–511.
[15] Farshbar-Shaker MH, Heinemann C. A phase field approach for optimal boundary control of damage processes in two-dimensional viscoelastic media. Math Mod Meth Appl S 2015;25:2749–93.
[16] Zhou S, Wang M. Multimaterial structural topology optimization with a generalized Cahn–Hilliard model of multiphase transition. Struct Multidisc Optim 2007;33:89–111.
[17] Hilforst D, Kampmann J, Nguyen TN, van der ZKG. Formal asymptotic limit of a diffuse-interface tumor-growth model. Math Mod Meth Appl S 2015;25:1011–43.
[18] Wise SM, Lowengrub JS, Frieboes HB, Cristini V. Three-dimensional multispecies nonlinear tumor growth-i: model and numerical method. J Theor Biol 2008;253:524–43.
[19] Dehghan M, Mohammadi V. Comparison between two meshless methods based on collocation technique for the numerical solution of four-species tumor growth model. Commun Nonlinear Sci Numer Simul 2017;44:204–19.
[20] Dehghan M, Mohammadi V. The numerical solution of Cahn-Hilliard (CH) equation in one, two and three-dimensions via globally radial basis functions (GRBFs) and RBFs-differential quadrature (RBFs-DQ) methods. Eng Anal Bound Elem 2015;51:74–100.
[21] Dehghan M, Abbaszadeh M. The meshless local collocation method for solving multi-dimensional Cahn–Hilliard, Swift–Hohenberg and phase field crystal equations. Eng Anal Bound Elem 2017;78:49–64.
[22] Dehghan M, Mirzaei D. A numerical method based on the boundary integral equation and dual reciprocity methods for one-dimensional Cahn-Hilliard equation. Eng Anal Bound Elem 2009;33:522–8.
[23] Elliott CM, French DA. Numerical studies of the Cahn–Hilliard equation for phase separation. IMA J Appl Math 1987;38:97–128.
[24] Gomez H, Calo VM, Bazilevs Y, Hughes TJ. Isogeometric analysis of the Cahn–Hilliard phase-field model. Comput Meth Appl Mech Eng 2008;197:4333–52.
[25] Wells GN, Ellen K, Krishna G. A discontinuous Galerkin method for the Cahn–Hilliard equation. J Comput Phys 2006;218:860–77.
[26] He Y, Liu Y, Tang T. On large time-stepping methods for the Cahn–Hilliard equation. Appl Numer Math 2007;57:616–28.
[27] Zhu J, Chen LQ, Shen J, Tikare V. Coarsening kinetics from a variable mobility Cahn–Hilliard equation-application of semi-implicit fourier spectral method. Phys Rev E 1999;60:3564–72.
[28] Ye X, Cheng X. The fourier spectral method for the Cahn–Hilliard equation. Appl Math Comput 2005;;171:345–57.
[29] He L, Yunxian L. A class of stable spectral methods for the Cahn–Hilliard equation. J Comput Phys 2009;228:5101–10.
[30] De Mello E, da Silveira Filho OT. Numerical study of the Cahn–Hilliard equations in one, two and three dimensions. Physica A 2005;347:429–33.
[31] Furihata D. A stable and conservative finite difference scheme for the Cahn–Hilliard equation. Numer Math 2001;87:675–99.
[32] Zhang Z, Qiao Z. An adaptive time-stepping strategy for the Cahn–Hilliard equation. Commun Comput Phys 2012;11:1261–78.
[33] Kim JS. A numerical method for the Cahn–Hilliard equation with a variable mobility. Commun Nonlinear Sci Numer Simul 2007;12:1560–71.
[34] Choo SM, Chung SK. Conservative nonlinear difference scheme for the Cahn–Hilliard equation. Comput Math Appl 1998;36:31–9.
[35] Ceniceros HD, Alexandre MR. A nonstiff, adaptive mesh refinement-based method for the Cahn–Hilliard equation. J Comput Phys 2007;225:1849–62.
[36] Wodo O, Baskar G. Computationally efficient solution to the Cahn–Hilliard equation: adaptive implicit time schemes, mesh sensitivity analysis and the 3d isoperimetric problem. J Comput Phys 2011;230:6037–60.
[37] Jokisaari AM, Voorheesa PW, Guyer JE, Warren J, Heinonen OG. Benchmark problems for numerical implementations of phase field models. Comp Mater Sci 2017;126:139–51.
[38] Ratz A. A benchmark for the surface Cahn–Hilliard equation. Appl Math Lett 2016;56:65–71.
[39] Tomé MF, Castelo A, Murakami J, Cuminato JA, Minghim R, Oliveira MC, Mangiavacchi N, McKee S. Numerical simulation of axisymmetric free surface flows. J Comput Phys 2000;157:441–72.
[40] Eyre D.J.. An unconditionally stable one-step scheme for gradient systems, 1997, Preprint, http://www.math.utah.edu/~eyre/research/methods/stable.ps.
[41] Choi JW, Lee HG, Jeong D, Kim JS. An unconditionally gradient stable numerical method for solving the Allen–Cahn equation. Physica A 2009;388:1791–803.
[42] Eyre DJ. Computational and mathematical models of microstructural evolution. Warrendale, PA: The Material Research Society; 1998.
[43] Trottenberg U, Oosterlee C, Schüller A. Multigrid. London: Academic Press; 2001.
[44] Kim J, Kang K, Lowengrub J. Conservative multigrid methods for Cahn-Hilliard fluids. J Comput Phys 2004;193:511–43.
[45] Aland S, Voigt A. Benchmark computations of diffuse interface models for two-dimensional bubble dynamics. Int J Numer Methods Fluids 2012;69:747–61.